

Highlights

Predicting cement microstructure and mechanical properties in hydrating cement paste with a Phase-Field model

Alexandre Sac-Morane, Katerina Ioannidou, Manolis Veveakis, Hadrien Rattiez

- A physics-based Phase-Field model predicts the microstructure evolution during the hydration of cement-based material.
- Predicted microstructures are used to derive the elastic moduli of the composite material with a computational homogenization scheme.
- Predicted microstructures and elastic moduli show excellent agreement with data available in the literature.

Predicting cement microstructure and mechanical properties in hydrating cement paste with a Phase-Field model

Alexandre Sac-Morane^{a,b,c,*}, Katerina Ioannidou^d, Manolis Veveakis^a,
Hadrien Rattez^b

^a*Multiphysics Geomechanics Lab, Duke University, Hudson Hall Annex, Room No. 053A, Durham, 27708, NC, USA*

^b*Institute of Mechanics, Materials and Civil Engineering, UCLouvain, Place du Levant 1, Louvain-la-Neuve, 1348, Belgium*

^c*Laboratoire Navier, ENPC, Institut Polytechnique de Paris, Univ Gustave Eiffel, 12 boulevard Copernic, Champs-sur-Marne, 77420, France*

^d*Laboratory of Mechanics and Civil Engineering, University of Montpellier, 860 Rue de St-Priest, Montpellier, 34090, France*

Abstract

Predicting the evolving microstructure of hydrating cement is essential for understanding and modeling its mechanical property development. Physics-based continuum approaches offer a rigorous framework for capturing the thermodynamics of dissolution and precipitation processes at the microstructural scale. In this work, we present an adapted Phase-Field (PF) model for cement hydration that resolves key physical inconsistencies in existing PF formulations by introducing a revised free-energy potential and distinct equilibrium constants for clinker dissolution and hydrate precipitation. The

*Corresponding author

Email addresses: alexandre.sac-morane@enpc.fr (Alexandre Sac-Morane),
aikaterini.ioannidou@umontpellier.fr (Katerina Ioannidou),
manolis.veveakis@duke.edu (Manolis Veveakis), hadrien.rattez@uclouvain.be
(Hadrien Rattez)

resulting PF framework reproduces microstructural evolution, yielding realistic porosity levels and continuous phase boundaries in close agreement with experimental observations.

The predicted hydrated microstructures are subsequently used in a computational homogenization scheme to evaluate the elastic response of the material. The PF-derived mechanical properties show good agreement with experimental trends, supporting the ability of the proposed framework to consistently link hydration chemistry, microstructure formation, and the resulting mechanical response.

Keywords: Cement hydration, Microstructure evolution, Phase-Field, Computational homogenization

1. Introduction

A central objective in the study of cement-based materials is to elucidate and predict their mechanical behavior [1], in order to enable the optimization of existing formulations or the development of alternative binders [2], particularly those with reduced environmental impact. Over the past decades, numerous analytical and empirical models have been proposed to capture the wide range of factors governing the mechanical performance of cementitious systems [3, 4, 1]. These factors include, among others, the water-to-cement mass ratio (w/c), raw material properties, particle size distribution, and the presence of chemical or mineral additives [5, 6, 7, 8, 9].

Beyond these empirical formulations, foundational physical models were developed to describe the evolution of the hydrate microstructure. The Powers–Brownyard model [10] provided the first quantitative framework for the

structure of hydrated cement paste, distinguishing between gel pores and capillary pores. Later, idealized microstructures were described using homogenization approaches, involving three steps—description, localization, and upscaling—to relate microscale phase morphology to macroscale mechanical properties [11, 12]. A variety of homogenization schemes have been proposed [13, 14, 15, 16, 17], with the dilute [18], self-consistent [19], and Mori–Tanaka [20] approaches being the most widely adopted. Such schemes can be concatenated across multiple scales—from hydrate foam (20 μm) to cement paste (0.7 mm), and from cement paste to mortar (1 cm) [21, 22, 23]. Coupling these approaches with hydration kinetics enables the prediction of evolving mechanical properties throughout hydration [24]. These efforts established the conceptual link between hydration degree, porosity, and mechanical performance—a relationship modern computational models now aim to simulate explicitly [25]. Nonetheless, these homogenization methods rely on idealized or simplified microstructures.

To overcome such limitations, microstructure-explicit hydration models were developed. One of the earliest is HYMOSTRUC [26], where reactants and products are idealized as continuum spheres whose sizes evolve during dissolution or precipitation. This framework was later extended to voxel-based microstructures in CEMHYD3D [27], where hydration is simulated through Cellular Automata (CA). Although widely used, CA approaches are constrained by voxel resolution. To alleviate this limitation, alternative solvers such as HydratiCA [28], μic [29], and the Integrated Particle Kinetics Model [30] were introduced. However, all those methods are based on semi-empirical reaction coefficients.

More recently, level-set based approaches were proposed to describe microstructure evolution using continuous fields and physics-based dissolution–precipitation laws [31]. Although these methods incorporate fundamental hydration kinetics, the underlying Kooi law [32] is formulated at the macroscale and does not strictly satisfy local physical constraints at the microstructural scale.

To address this issue, Phase-Field (PF) methods have emerged as a promising alternative [33]. PF formulations naturally describe interface evolution based on local thermodynamic principles and have been successfully applied to various dissolution/precipitation [34, 35, 36, 37, 38, 39] and fracture problems [40, 41, 42]. When coupled with diffusion equations for dilute species, PF models enable dissolution and precipitation to occur whenever local solute concentrations deviate from their equilibrium values, thus ensuring thermodynamic consistency at the microstructural scale.

However, the formulation introduced in [33] presents two limitations that motivate the present work. First, the free-energy functional employed permits spontaneous gel precipitation even when the system is at equilibrium. Second, the equilibrium concentrations associated with source–solute (dissolution) and solute–gel (precipitation) reactions are assumed equal, whereas they are known to be distinct according to established hydration theory [43, 44]. These inconsistencies hinder the model’s physical fidelity and predictive capability. To address these issues, the present work proposes an adapted Phase-Field formulation in which the free-energy landscape and equilibrium relationships are revised to better reflect the thermodynamics of cement hydration.

Once the hydrated microstructure has been computed, the mechanical

behavior of the hardened cement-based material can be determined using computational homogenization. This permits the calculation of properties such as Young’s modulus, shear modulus, Poisson’s ratio, bulk modulus, and strength parameters, which depend explicitly on microstructural morphology and hydration state [45, 46]. The phases (pore, skeleton, binder) can be distinguished and characterized based on their intrinsic properties. The composite microstructure is then subjected to a Finite Element or Fast Fourier Transform-based homogenization scheme to infer macroscale mechanical parameters [47, 48, 49].

The contribution of this work is organized as follows. First, the formulation of the adapted PF model for cement hydration is presented. The framework is then applied to boundary-value problems for $w/c = 0.3$ and 0.5 . The microstructural evolution predicted by the model is compared with results from CEMHYD3D [48] and with experimental measurements [6, 50]. Finally, the resulting hydrated microstructures are subjected to mechanical loading (shear and tension) in order to estimate mechanical properties such as Young’s and shear moduli, which are compared to values reported in the literature, particularly those in [48].

2. Formulation of the microstructure evolution

This section focuses on the modelization of the microstructure evolution during hydration. This chemical process is divided into two main reactions: dissolution and precipitation. The source phases (mainly C_3S , C_2S , C_3A and C_4AF) react with water and dissolve [51, 52]. The generated solute diffuses and is consumed during the precipitation of the phases of the cement paste

(mainly calcium silicate hydrates C-S-H and Portlandite CH) [51, 52]. For simplicity reasons, only three phases are considered in this paper: the source (C_3S) which is the main clinker phase of Portland cement [52, 53], the paste of the cement (C-S-H), which represents the main product of the hydration [48, 52], and the solute (c), which is a transient specie dissolved in the water. As shown in Figure 1, C_3S dissolves to generate c , and c is consumed to generate C-S-H after its diffusion. In the same vein of simplification, the local packing fraction of the C-S-H is considered constant and homogeneous in the precipitated phase. This assumption is a limitation compared to the observations showing that this property is heterogeneous and evolves with the hydration process [54, 55, 56]. These hypotheses are a common and effective first-order approximation for estimating the evolution of bulk elastic properties, which is the primary focus of this investigation. Of course, the framework presented herein can be extended to the other phases and to an evolving local packing fraction for the C-S-H.

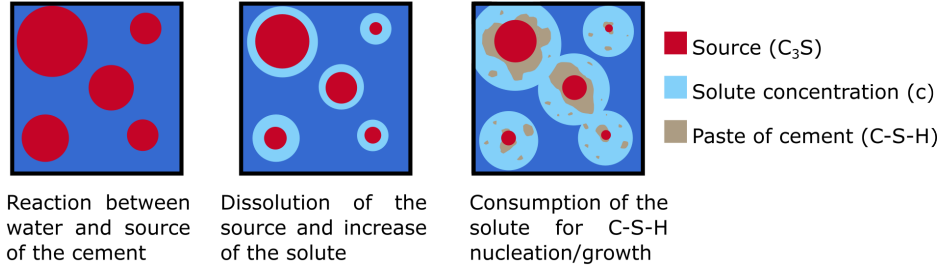


Figure 1: Scheme of the hydration process considered.

In the following sections, the equations solved and the numerical model are presented. Then, a validation of the microstructure is performed by comparison with the literature [6, 48, 50].

2.1. Equations solved

Three coupled equations are solved with a finite element solver MOOSE [57, 58]. Equations 1 and 2 are Allen-Cahn formulations [59] applied to the phase variables $C3S$ (the source of the cement) and CSH (the cement paste) to model heterogeneous dissolution/precipitation phenomena [38, 39]. The variable $C3S$ (resp. CSH) equals 1 if it is located inside a source of cement (resp. the C-S-H gel) and equals 0 elsewhere. In the following of this article, a variable η can be used, representing the variables $C3S$ or CSH . In parallel, Equation 3 is a diffusive equation applied to the variable c . This variable represents the solute concentration in the water of the dilute species.

$$\frac{\partial C3S}{\partial t} = -L_{C3S} \frac{\partial f_{C3S} + Ed}{\partial C3S} + L_{C3S} \kappa_{C3S} \nabla^2 C3S \quad (1)$$

$$\frac{\partial CSH}{\partial t} = -L_{CSH} \frac{\partial f_{CSH} + Ep}{\partial CSH} + L_{CSH} \kappa_{CSH} \nabla^2 CSH \quad (2)$$

$$\frac{\partial c}{\partial t} = -\alpha_{CSH} \frac{\partial CSH}{\partial t} - \alpha_{C3S} \frac{\partial C3S}{\partial t} + \kappa_c \nabla^2 c \quad (3)$$

Where, L_η is the effective mobility of the phase η (impacting the kinetics of the relation, $= 1$ here), κ_η is the gradient coefficient of the phase η (influencing the width of the phase interface), f_η is the free energy of the phase η , Ed/Ep are the tilting free energies. The formulation of the free energies $f_\eta/Ed/Ep$ is described in Section 2.2. Finally, κ_c is the diffusivity of the solute concentration c , defined Equation 4 [33].

$$\kappa_c = \kappa_{c0} (1 - C3S) \exp(-\kappa_{cexp} CSH) \quad (4)$$

Where, the term $1 - C3S$ is a penalty term to avoid diffusion of the solute in the source of cement. Similarly, the term $\exp(-\kappa_{cexp} CSH)$ models the

decrease of the diffusivity of the solute in the gel [60, 61], where κ_{cexp} is the penalty coefficient. A factor $\exp(-\kappa_{cexp}) = 1/400$ is used [62].

Furthermore, the gradient coefficient κ_η is related to the free energy f_η described in Section 2.2 [35, 39].

$$\kappa_\eta \propto W_\eta \cdot \delta^2 \quad (5)$$

Usually, $\delta = 4\Delta - 10\Delta$ [34, 35], where Δ is the mesh discretization. W_η is the energy barrier of the free energy f_η , see Equation 7. Even if a strong mesh dependency exists because of the PF definition, a method to cancel this impact is detailed in [39].

The terms $\frac{\partial c}{\partial t} = -\alpha_{CSH} \frac{\partial CSH}{\partial t} - \alpha_{C3S} \frac{\partial C3S}{\partial t}$ of the Equation 3 ensure the conservation of the total mass [33, 38, 39]. The coefficients α_{CSH} and α_{C3S} represent conversion terms (1η gives $\alpha_\eta c$). These coefficients can be determined with the mass conservation between the initial \cdot_i and the final \cdot_f configurations at the saturation limit, see Equation 6. The saturation limit is defined as the total consumption of the source particles and the entire saturation of the domain by the C-S-H gel.

$$\alpha_{C3S} C3S_i + \alpha_{CSH} CSH_i + c_i = \alpha_{C3S} C3S_f + \alpha_{CSH} CSH_f + c_f \quad (6)$$

With:

- $C3S_i = 1/2.344$, here the saturation is assumed at $(w/c)_{sat} = 0.42 \iff \frac{1-C3S_i}{C3S_i} \frac{\rho_{H2O}}{\rho_{C3S}} = 0.42$, with w the mass of water, c the mass of the source, and $\rho_{H2O}/\rho_{C3S} = 1000/3200$ [33].

- $CSH_i = 0$, there is no C-S-H gel in the initial state (except some insignificant nucleation seeds).
- $c_i = c_{eq, CSH}$, the solute concentration is at equilibrium with the C-S-H gel in the initial state.
- $C3S_f = 0$, there is no source of cement in the final state, ensuring the full hydration.
- $CSH_f = 1$, the domain is fully saturated with the C-S-H gel in the final state, ensuring the full hydration.
- $c_f = c_{eq, C3S}$, the solute concentration is at equilibrium with the source of cement C3S in the final state, ensuring the full hydration.

By the nature of the problem, the equilibrium constants $c_{eq, C3S}$ and $c_{eq, CSH}$ must be different [43, 44]. Furthermore, it appears that $c_{eq, C3S}$ is several orders of magnitude larger than $c_{eq, CSH}$ [52]. Thus, it can be assumed that $c_{eq, C3S} = 1$ and $c_{eq, CSH} = 0$. Injecting these assumptions into the Equation 6 and assuming $\alpha_{CSH} = 3$, it gives $\alpha_{C3S} = 9.376$. It is important to notice that the value of the coefficient α_{CSH} has been found after a sensitivity analysis available in Appendix B. Indeed, this coefficient affects the conversion term α_{C3S} between the source $C3S$ and the solute c during the dissolution. If the value is too small, the solute c produced is not large enough to saturate the pore fluid, and the supersaturation state observed in experiments is not verified [43, 44]. Similarly, the consequence of a small α_{CSH} coefficient is the fact that the source particles are significantly dissolved before the precipitation of the paste, not in agreement with the experimental observations.

2.2. Tilting the free energy f_η to obtain dissolution/precipitation

In this description, the source of cement is modeled by the phase variable $C3S$. In a similar vein, the C-S-H gel is modeled by the phase variable CSH . As a reminder, a variable η can be employed herein to refer to $C3S$ or CSH . As emphasized by the Allen-Cahn formulation detailed in Equations 1 and 2, a free energy f_η is employed to describe the problem. The equilibrium is reached in the system when the free energy is minimized. In the literature different expressions are available [33, 35, 63, 64], but a double well one is preferred, as the minimum locations are fixed and known. Furthermore, it appears to be the most used form in the literature. The formulation of this function is given Equation 7 and is illustrated in Figure 2.

$$f_\eta(\eta) = W_\eta \times \eta^2(1 - \eta)^2 \quad (7)$$

Where, W_η is the barrier energy of the phase variable η ($= 1$ here), preventing phase transformation.

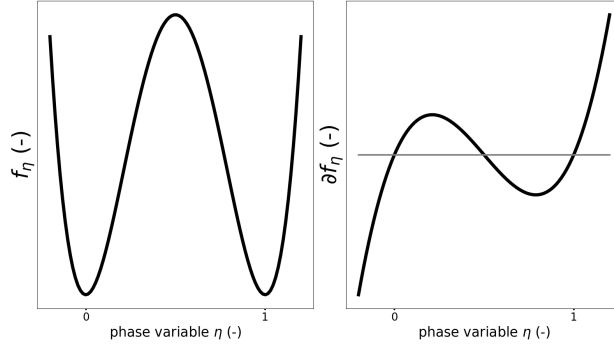


Figure 2: Free energy f_η and its derivative ∂f_η .

It is important to notice that the minima of this potential energy are located at $\eta = 0$ and $\eta = 1$. Then, these values are used to describe the source

and the gel. As the PF description minimizes the free energy in the domain, the phase variable remains at these values at the equilibrium and without external destabilization. There is no dissolution/precipitation. Subsequently, the idea is to add an external source term Ed/Ep to tilt the initial free energy to favor localized dissolution or precipitation [33, 36, 38, 39]. Indeed, depending on the tilting, $\eta = 0/1$ is no longer the minimum of the free energy, and some dissolution/precipitation occurs. These tilting free energy functions are defined Equations 8 and 9.

$$Ed(c, C3S) = \chi_{c,C3S} \times (c_{eq,C3S} - c) \times h_{C3S}(C3S) \quad (8)$$

Where, $h_{C3S}(C3S) = 3C3S^2 - 2C3S^3$ is an interpolation function on the phase variable $C3S$ [35], $\chi_{c,C3S}$ is the tilting coefficient related to the dissolution kinetics. This coefficient can be calibrated with experimental data. The choice of the interpolation function h_{C3S} has an insignificant impact, while it verifies $h_{C3S}(0) = 0$, $h_{C3S}(1) = 1$, and $\frac{\partial h_{C3S}}{\partial C3S}(0) = \frac{\partial h_{C3S}}{\partial C3S}(1) = 0$. For instance, other formulations have been employed in [33]. It is important to notice the tilt occurs only if $c \neq c_{eq,C3S}$ and dissolution occurs in the case $c < c_{eq,C3S}$. The value $c_{eq,C3S} = 1$ is considered for the equilibrium for the source dissolution. Figure 3 illustrates an example of tilting. It is important to point out that the term $\chi_{c,C3S} \times (c_{eq,C3S} - c)$ determines the amplitude of the tilting, and so the kinetics of the dissolution. The larger the tilting is, the faster the dissolution is.

$$Ep(c, CSH) = \chi_{c,CSH} \times (c - c_{eq,CSH}) \times h_{CSH}(CSH) \quad (9)$$

Where, $h_{CSH}(CSH) = 1 - (3CSH^2 - 2CSH^3)$ is an interpolation function

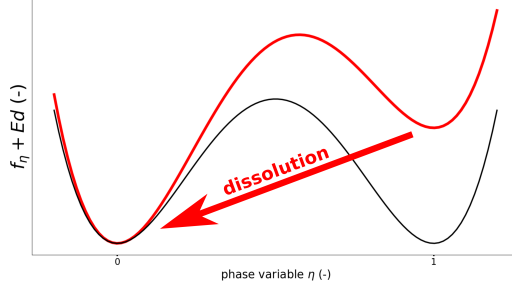


Figure 3: Example of tilted free energy $f_{C3S} + Ed(c, C3S)$ (in red), the dissolution is favored ($c < c_{eq, C3S}$).

on the phase variable CSH [35], $\chi_{c, CSH}$ is the tilting coefficient related to the precipitation kinetics. This coefficient can be calibrated with experimental data. Similarly, the choice of the interpolation function h_{CSH} has an insignificant impact, while it verifies $h_{CSH}(0) = 1$, $h_{CSH}(1) = 0$, and $\frac{\partial h_{CSH}}{\partial CSH}(0) = \frac{\partial h_{CSH}}{\partial CSH}(1) = 0$. It is important to notice the tilt occurs only if $c \neq c_{eq, CSH}$ and precipitation occurs in the case $c > c_{eq, CSH}$. The value $c_{eq, CSH} = 0$ is considered for the equilibrium for the C-S-H precipitation. Figure 4 illustrates an example of tilting. It is important to point out that the term $\chi_{c, CSH} \times (c - c_{eq, CSH})$ determines the amplitude of the tilting, and so the kinetics of the precipitation. The larger the tilting is, the faster the precipitation is.

Even if the model can predict the distribution of the volume fractions of the different phases in the domain, it is worth noting that the chemical shrinkage is not captured herein. This phenomenon is defined as a reduction of the source+paste+water volume and an increase of the air volume (in proportion to conserve the volume of the sample) [10]. For simplicity reasons, the air phase is neglected and the domain is assumed to be always saturated

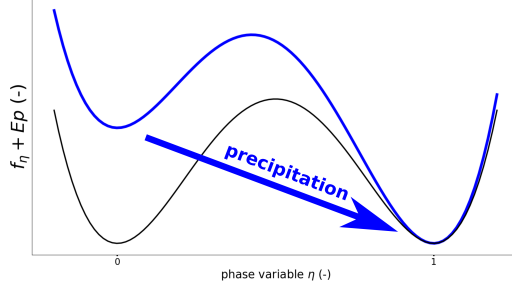


Figure 4: Example of tilted free energy $f_{CSH} + Ep(c, CSH)$ (in blue), the precipitation is favored ($c > c_{eq, CSH}$).

(addition of water during the hydration). Indeed, the effect of the shrinkage (and the required addition of water) remains small during the hydration phenomenon.

The PF framework with dissolution/precipitation is then ready to be employed to predict the microstructure evolution.

3. Numerical microstructure evolution

Similarly to [48], two configurations are considered, employing a $100 \mu m$ domain size: $w/c = 0.3$ and $w/c = 0.5$. Indeed, a saturation limit $w/c = 0.42$ has been assumed to formulate the problem in Equation 6, and the under- and over-saturation configurations are explored. Even if the framework is easily extended to 3D, only 2D slices have been considered in this paper. Indeed, the PF description can be computationally expensive.

The different parameters are available in Table 1. Considering the lack of information on the value of the tilting coefficients $\chi_{c, CSH}/\chi_{c, C3S}$, they have been assumed equal. Moreover, the competition between precipitation/dissolution $\chi_{c, CSH}/\chi_{c, C3S}$ and diffusion κ_{c0} is primordial. Indeed, the

slowest physics determines the global hydration kinetics. It appears that the diffusion in the C-S-H gel dictates the rate of the hydration reactions [43, 44]. This diffusivity value κ_{c0} is uncertain and has been determined by a trial-and-error method to correlate data from [48]. At the contrary, the values of the tilting coefficients $\chi_{c,CSH}/\chi_{c,C3S}$ have an insignificant impact on the results as the precipitation/dissolution physics is faster than the diffusion.

The mesh size ($0.2 \mu m$) has been determined to limit the computation cost induced by the PF description, while ensuring the quality of the result. Such as comparison, a mesh size of $1 \mu m$ is employed in the CA formulation [48]. To investigate if the modelization is representative, at least ten simulations for each w/c configuration have been conducted.

Domain size	$100 \mu m$
Mesh size Δ	$0.2 \mu m$
Tilting coefficients $\chi_{c,C3S}/\chi_{c,CSH}$	$0.1 W_\eta$
Diffusivity κ_{c0}	$1 \mu m^2$

Table 1: Parameters used during the microstructure evolution simulations.

3.1. Initial conditions

Spheres are generated in a periodic domain, considering a given particle size distribution function [9, 65] and a random position avoiding overlap. This particle size distribution is modified, see Appendix A, as the nature of the PF theory limits the size of the particles ($R_{min} \geq 12\Delta$, where Δ is the mesh size). Even if it is unclear in [48], such a modification seems also to be employed during the generation of the initial conditions for the CA approach.

Spheres are generated until the domain reaches the targeted ratio w/c . It is worth noting that sphere shapes have been used for simplification reasons. However, the PF formulation can capture any heterogeneous shape, such as the irregular shapes obtained during the microstructure evolution depicted in Figure 5.

Once the position of the source of cement has been determined, it is possible to determine the map of the phase variable $C3S$. A signed distance to the interface water-source is computed and a cosine profile is used [35], defined in Equation 10.

$$\begin{aligned}
 &= 1 \text{ if } d \leq -\delta/2 \text{ (inside the grain)} \\
 C3S &= 0.5 \left(1 + \cos \left(\pi \frac{d + \delta/2}{\delta} \right) \right) \text{ if } |d| < \delta/2 \text{ (in the interface of the grain)} \\
 &= 0 \text{ if } d \geq \delta/2 \text{ (outside the grain)}
 \end{aligned} \tag{10}$$

Where, d is the signed ($-$ if inside the grain, $+$ if outside the grain) distance of the node to the interface and δ is the interface thickness.

Concerning the map of the phase variable CSH , one would like to set $CSH = 0$ (no gel) everywhere. Then, the gel needs to nucleate and propagate with the consumption of the solute c . Nevertheless, PF formulation has some difficulties in capturing the nucleation phenomenon, in particular if it is localized. The physical mechanisms governing the initial formation of C-S-H are known to be complex, involving processes like frustrated nucleation and growth. To ensure the localization of the nucleation around the source particle [51, 52], a given number of nucleation seeds are therefore generated

in the simulation. The same strategy was used in Molecular Dynamics precipitation simulations for the nucleation and growth of C-S-H [55, 66]. Their positions are randomly selected in the source neighborhood. Then, a cosine profile, see Equation 10, is applied with a radius of several mesh sizes. Furthermore, some noise is introduced into Equation 2 to obtain heterogeneous nucleation/growing due to imperfections or temperature fluctuations [33, 67].

Finally, the solute concentration c is set to $c_{eq, CSH} = 0$ in the domain, the value of the gel-water equilibrium. Without source grain, the domain is at the equilibrium. After the introduction of the source in the domain, dissolution occurs as the source-water equilibrium is not verified ($c = 0$ versus $c_{eq, C3S} = 1$). The consequence of this dissolution is the increase of the solute concentration c in the domain. With $c > c_{eq, CSH}$, the gel-water equilibrium becomes not verified, and precipitation occurs. As depicted in Figure 1, these processes verify the hydration phenomenon.

3.2. Results

Figure 5 depicts examples of microstructure evolution, and different movies are available in supplementary documents. As expected, the source phase dissolves to produce the gel phase. Occasionally, a source grain may become entrapped within the cementitious matrix, subsequently acting as an inclusion within the hardened paste. Indeed, the solute generated from the source dissolution is trapped in the paste. Remember that the diffusivity of the solute is much smaller in the paste than in the pore [43, 44, 68], see Equation 4. As the solute is trapped, the solute concentration c reaches the equilibrium value of the dissolution reaction $c_{eq, C3S}$, and the dissolution stops locally. Furthermore, it appears the paste is not the only phase to precipitate (see at

the bottom for $w/c = 0.3$ in Figure 5). Indeed, the source phase precipitates also. The PF theory can induce curvature-driven shape evolution to reduce surface tension [34, 59]. The origin of this unphysical phase evolution is the gradient coefficient κ_η from Equations 1 and 2. The solution to this problem appears to be the use of new distinct phase variables for each grain, increasing the computational cost [38]. The volume fraction of this reprecipitated source was found to be less than 0.3% in all simulations (mean value of 0.1%) and thus has a minimal effect on the overall phase fractions and computed mechanical properties.

It is worth noting that microstructures from Figure 5 have not reached the final configuration. Indeed, some chemical reactions occur until the total consumption of the source particle (for the undersaturated configuration, $w/c = 0.5$) or until the saturation state is reached (for the oversaturated configuration, $w/c = 0.3$). However, the hydration kinetics are strongly slowed down by the trapping of the solute in the paste. The final configurations depicted herein are expected to be a sufficient approximation of the steady state.

Compared to microstructures obtained with a *CEMHYD3D* model [48] or observed after a real hydration experiment [6], the phase boundaries are smoother and the integrity of the phases is conserved in the PF framework. Indeed, the PF framework has been observed to facilitate the smoothing of interfaces [69], which may lead to the inaccurate capture of the fingering growth pattern [6]. A finer mesh would help to capture heterogeneous shapes, increasing the computational cost.

This chemical process can be described by the degree of hydration of the

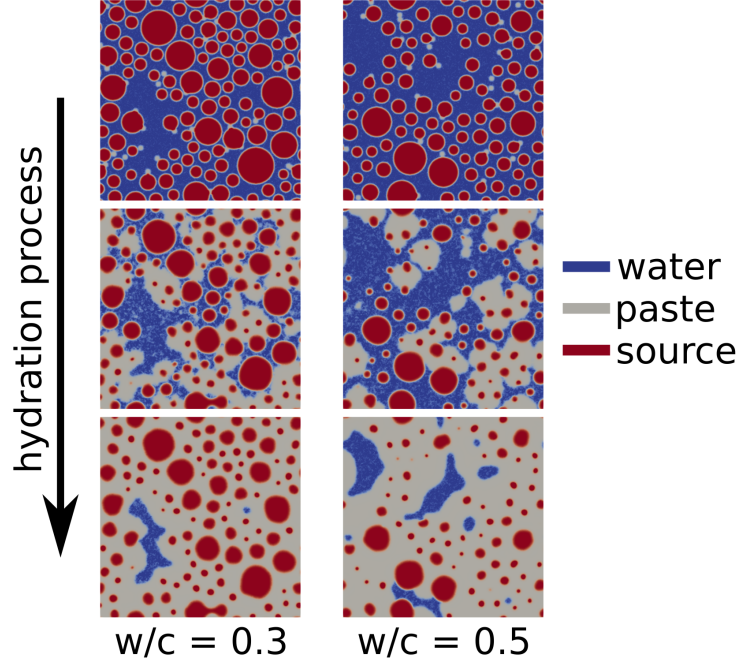


Figure 5: Evolution of the microstructure during the hydration process.

source material h , defined in Equation 11. This index varies between 0 for intact source particles initially to 1 when all the source phases are dissolved.

$$h = \frac{C3S_i - C3S_t}{C3S_i} \quad (11)$$

Where, $C3S_i$ and $C3S_t$ are the source variable's initial and current mean values.

Figure 6 shows the evolution of the hydration in the two cases ($w/c = 0.3$ and 0.5). The results are compared to the hydration curves obtained with the CA description in [48] and to experimental results obtained with $w/c = 0.4$ and $= 0.55$ [50]. The time has been normalized to allow the comparison between the results. Considering the repetitions of the configurations, Figure

6 depicts the average value in plain lines and an envelope in the color areas. This envelope considers the extrema values $\mu - \sigma$ and $\mu + \sigma$, where μ is the mean value and σ is the variance at a given x-coordinate. This representation is preserved in the following of this work.

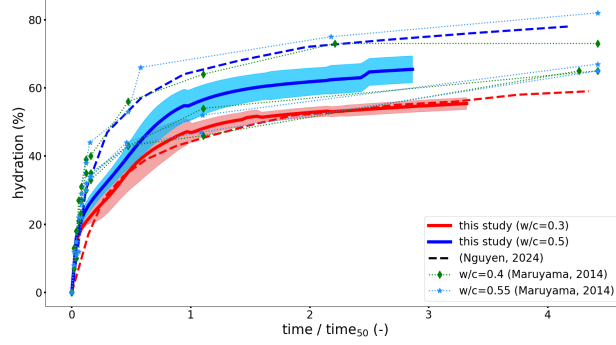


Figure 6: Time evolution of the degree of hydration in the distinct cases (configurations are repeated ten times). $time_{50}$ is the normalization factor defined as the mean time required to reach $h = 50\%$.

Hydration appears to be divided into two parts: a fast dissolution period and a slow dissolution period [43, 44, 68]. In the first part of the curve, dissolution occurs. However, the diffusivity of the solute aims to decrease with the precipitation of the C-S-H, and the solute concentration locally reaches the water-source equilibrium value. This phenomenon slows down the dissolution of the source, explaining the second part of the curve. As expected, the hydration kinetics are faster for the configuration $w/c = 0.5$ than for $w/c = 0.3$. Indeed, $w/c = 0.5$ is an under-saturation configuration, and the dissolution of the source particles is favored. The results from the PF simulations appear to correlate well with the CA prediction and with the experimental observations (even if the w/c are not similar). About the

representativeness of the simulations, the results for the $w/c = 0.3$ configuration are strongly similar. In the same vein, the results for the $w/c = 0.5$ configuration appear reproducible, even if the variance is a bit larger. This aspect can be diminished, considering a larger domain size. In the following, the $100\,\mu m$ domain is conserved for comparison purposes with [48].

Then, the microstructure evolution can be described through the evolution of the volume fractions of the different species, see Figure 7. The hydration phenomenon is well divided into the dissolution of the source to generate some solute and then the consumption of the solute to precipitate the paste, with an intermediary supersaturation of the pore space with respect to the gel.

If the mean value of the source quantity appears similar to the one obtained by [48] (C_3S , C_2S , C_3A , C_4AF species are considered), it is not the case for the mean value of the paste quantity (CSH , CH species are considered), which is larger in the PF simulations. Even if supplementary phases (available in [48]) were included such as the gypsum, the anhydrite, the ettringite, the AFm or FH_3 , these phases represent only $\sim 19\%$ of the volume for $w/c = 0.3$ and $\sim 16\%$ of the volume for $w/c = 0.5$ [70]. It is not sufficient to fill the gap between the PF and the CA descriptions. In order to determine the most accurate formulation, the final concentrations of the source and the paste obtained from the hydrated microstructure available in [6] ($w/c = 0.5$) are depicted for comparison. The results obtained with the PF description appear more accurate. It seems that *CEMHYD3D* simulations overestimate the pore space, in particular for the case $w/c = 0.5$. Furthermore, it is not possible to estimate the mean value of the solute concentration in the data

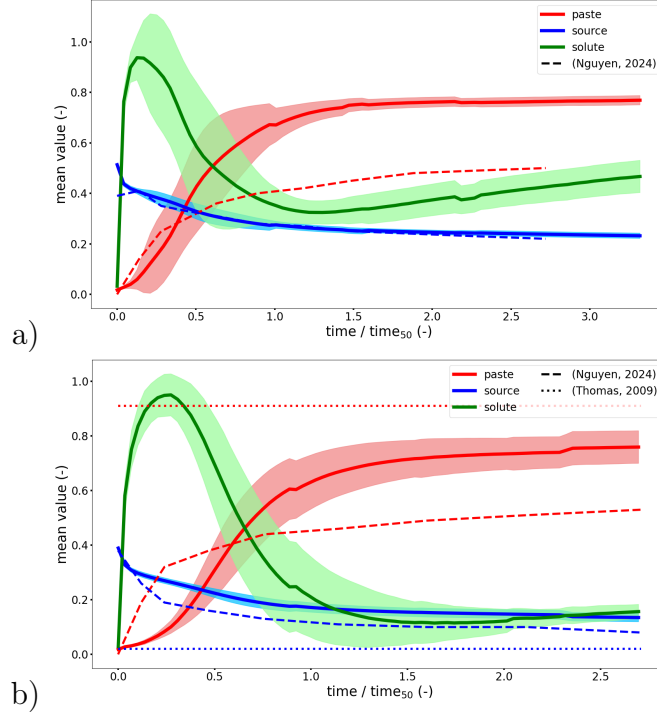


Figure 7: Time evolution of the different volume fractions for the species (source, paste, solute) in the case $w/c =$ a) 0.3 and b) 0.5 (configurations are repeated ten times).

described in [48]. Indeed, the *CEMHYD3D* description does not consider this specific phase. In the CA approach, the source phase is transformed directly into a paste phase if the chemical conditions are set (reaction between the given phases). Compared to the data from [48], a delay can be appreciated in the PF formulation concerning the precipitation of the paste, due to the required diffusion of the solute. Similarly to the hydration curves, the PF simulations appear reproducible in terms of phase distribution, in particular for $w/c = 0.3$. Beyond these bulk volume fractions, a deeper understanding of the microstructure's development can be gained by analyzing the morphology and spatial organization of the phases.

To do so, the microstructure is segmented into three phases: paste, source, and paste+source. The different nodes of the mesh are considered in the paste phase if $CSH > 0.5$. Similarly, the nodes are considered in the source phase if $C3S > 0.5$. The paste+source phase is a combination of the two previous phases. Then, the connectivity of the phases is quantified by labeling the different phases of the segmented images with the Python function *scipy.ndimage.label*. This operation distinguishes the individual features from a given phase. A feature is defined as a phase island surrounded by the pore/water. For instance, the number of features for the paste+source phase is depicted in Figure 8. It appears this number increases and then decreases as the source dissolves. The initial increase is due to the nucleation of the cement paste, while the reduction occurs as the source grains dissolve and the distinct paste seeds interconnect. It is worth noting the wide envelopes of this descriptor. Indeed, this specific morphometer remains at the microscale, counting the individual features, while the others consider a homogenization at the sample scale, computing an average value. It remains sensitive to the microstructure evolution, especially considering a domain size of $100\ \mu m$.

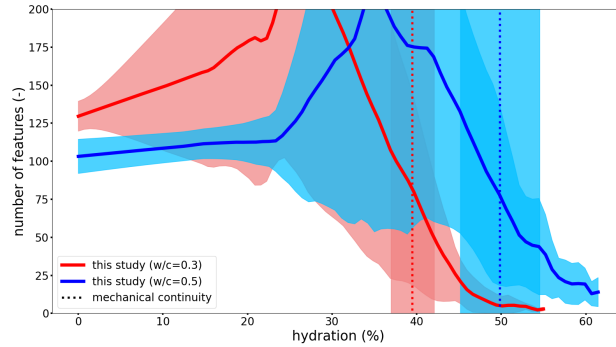


Figure 8: Evolution of the number of features for the phase paste+source.

The microstructure can be more deeply described by investigating the evolution of the perimeter of each phase (paste, source, paste+source), see Figure 9. This perimeter index is obtained by the function *measure.perimeter* from the Python module *skimage*.

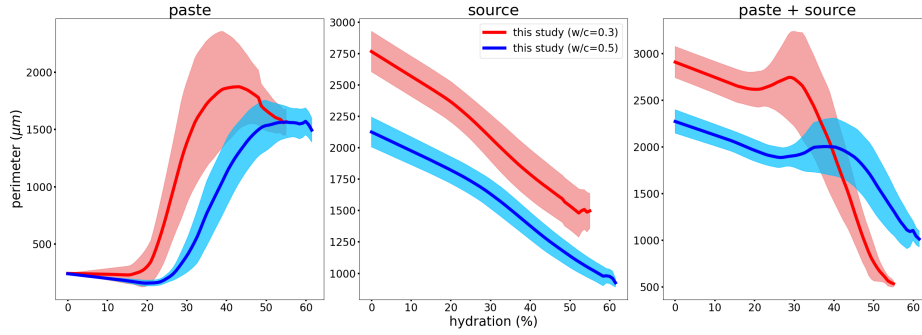


Figure 9: Evolution of the perimeter of the different phases (paste, source, paste+source) during the hydration (configurations are repeated ten times).

The perimeter of the source phase appears to decrease with the hydration (dissolution). On the contrary, the paste perimeter increases with the hydration (precipitation). Similarly to the phase distribution curves, the delay between the dissolution and the precipitation can be pointed out. Indeed, the perimeter of the paste does not evolve initially, while the perimeter of the source decreases, even at the initial times. Furthermore, a decrease in the paste perimeter during the hydration can be noticed at the end of the simulation. Indeed, as illustrated in Figures 5, the different paste seeds can interconnect, reducing the phase perimeter. This phenomenon also explains the slope variation of the paste+source perimeter curve. The decrease in the perimeter for the combined phase accelerates with the interconnection of the seeds. The nucleation and the coalescence of these aggregates are also

depicted in Figure 8, where the number of the distinct islands (paste+source phase surrounded by pore) shows an increase followed by a decrease during the hydration process. Similarly, Figure 7 and [55] emphasize the fact that the C-S-H volume fraction evolves with a sigmoidal pattern. While a direct overlay of the plots would be inappropriate as they measure different quantities (morphology vs. bulk volume), the non-monotonic hump shape of the perimeter curve is the direct morphological signature of the sigmoidal growth, revealing the nucleation/growing of separate islands followed by the coalescence of these aggregates. In the same vein as previously, the microstructure obtained with the PF formulation appears reproducible, regarding the size of the envelope.

Subsequently, these segmented images can be used to compute the normalized two-point correlation function, [71] and Appendix C for a definition, see Figure 10 (the results of only one simulation for $w/c = 0.3$ and $= 0.5$ are depicted for clarity reasons; however, the repeatability is discussed in Appendix D). This tool adds details on the structure of the microstructure by giving the characteristic size of the phase. Indeed, this function takes a value between 1 (highly correlated) and 0 (not correlated) for different length dimensions. For example, it appears the paste correlation function drops at the initial condition ($h \rightarrow 0$) for the distance equal to $5 \mu m$ (initial size of the seeds). Then, the correlation function increases for the different sizes as the paste phase precipitates. Similarly, the source correlation function decreases for all sizes with the hydration as the source dissolves. For comparison with the case $w/c = 0.5$, a real microstructure, from [6], is characterized. The phase paste+source appears well described by the PF formulation. It is

worth noting that the paste correlation is lightly underestimated, whereas the source correlation is lightly overestimated. These differences may be filled by considering a wider source size distribution or capturing the fingering growth pattern of the cement paste. Furthermore, the evolution of the two-point correlation function for the paste phase available in Figure 10 provides a quantitative signature of the developing microstructure. The progressive flattening of the curve at higher degrees of hydration indicates the establishment of long-range spatial correlations, which is the statistical marker of the percolation threshold. This signifies the physical transition of the paste from a collection of isolated aggregates into a continuous, sample-spanning network. This mechanism is also visible through the increase-decrease evolution of the paste perimeter, see Figure 9, and through the decrease of the number of isolated material islands, see Figure 8. This result is conceptually consistent with findings from more fundamental molecular dynamics studies of C-S-H formation, which also investigate the development of a cohesive, percolating gel network [54, 55]. The model’s ability to capture this critical topological transition therefore provides a validation of its physical realism.

Before the next Section, please note that other indices could have been applied to describe the microstructure [33, 45, 46, 72], such as the chord-length density function, the pore-size function, the Euler number, or the specific surface. These indices would characterize the microstructure with complementary information.

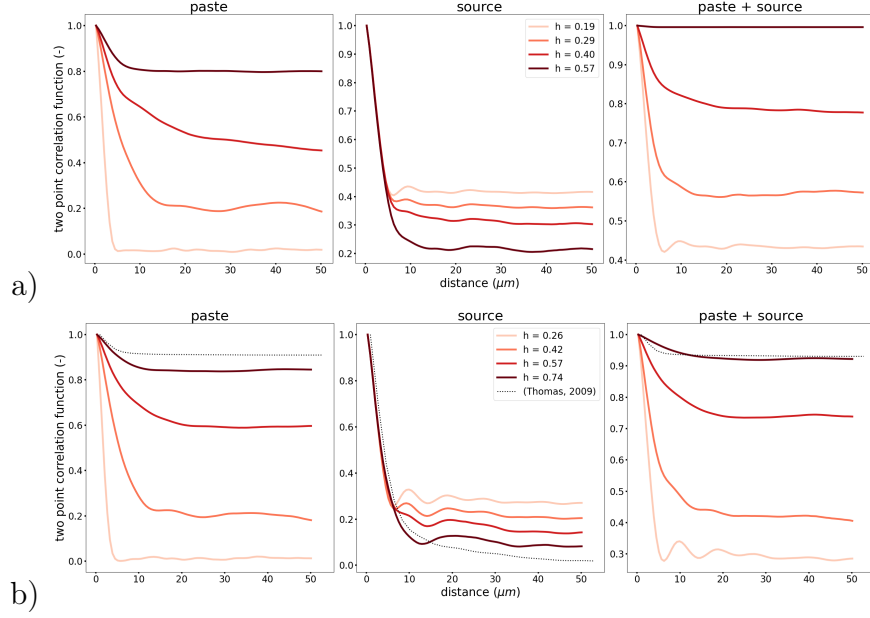


Figure 10: Evolution of the correlation function for the different phases (paste, source, paste+source) in the case $w/c =$ a) 0.3 and b) 0.5.

4. Mechanical characterization of the hydrated microstructure

4.1. Formulation of the mechanical homogenization

After estimating the microstructure evolution, mechanical loading (tensile and shear forces) is applied at the specimen's boundaries to determine the homogenized parameters, including Young's modulus and Shear modulus, see Figure 11. It is worth noting that the chemical aspect of the problem (microstructure evolution) is paused during this mechanical estimation of the composite material. The distinct microstructures obtained in Section 3 are employed as independent inputs in the following. Furthermore, the impact of the mechanics on the chemistry and microstructure evolution is neglected herein. However, this feedback influence is pivotal in some contexts,

such as the underground storage (involving hydrating concrete wells under stress [73, 74, 75]), and can be considered. For instance, a stress-dependent microstructure evolution has already been proposed in [36]. In the same vein, [38, 39] depicts the development of a new method to consider the impact of the stress and the microstructure reorganization on the chemistry.

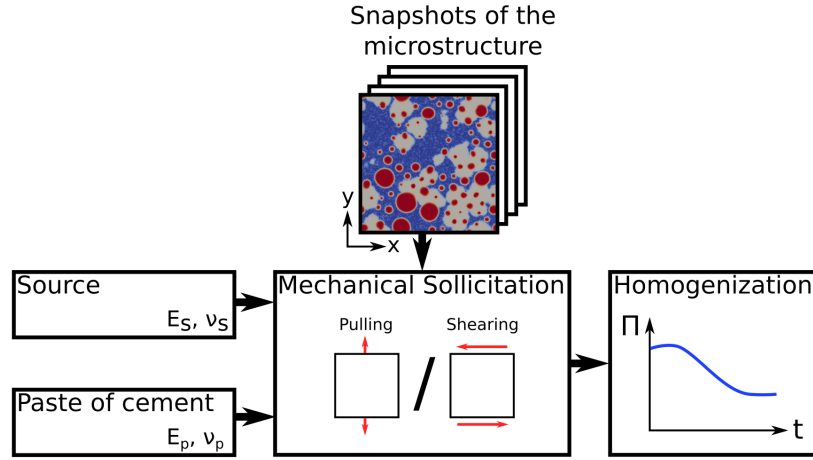


Figure 11: The microstructure is loaded to compute homogenized mechanical parameters.

A displacement (vertical in the case of pulling or lateral in the case of shearing) is applied on the top surface, whereas the bottom surface is assumed fixed. Periodic conditions are considered for the left and right surfaces to avoid any influence of the boundary conditions. It is worth noting that it is important to verify the mechanical continuity of the sample before the interpolation of the mechanical characteristics. To ensure force transmission between the top and bottom surfaces, the paste+source phase must be continuous, while the pore phase is not considered in the transmission of forces. Consequently, the initial microstructures formed during hydration are not used in the estimation of the sample's mechanical parameters as this crite-

tion is not verified. Figure 8 depicts the mean hydration (and its variation) ensuring the mechanical continuity.

Three phases are identified and assigned to the mesh: the paste, the source, and the water in the pore, all having an isotropic elastic mechanical behavior described in Table 2 [48, 54, 56, 70]. It is worth noting that the mechanical behavior of the paste has been simplified in this initial estimation. Indeed, it has been proved that the paste tends to behave such as a viscoelastic material, in particular at the early age [76, 77, 78]. Considering the intrinsic viscosity of the paste, the model would be able to predict the creep behavior of the hydrated cement. To ensure the water is not transmitting stress in the medium, the Young modulus assigned is small compared to the other phases. Hence, the stress will concentrate on the harder phases: the paste and the source.

Phase	Young modulus (GPa)	Poisson ratio (-)
Paste	25	0.24
Source	120	0.3
Pore	0.12	0.3

Table 2: Elastic properties considered for the different individual phases (from [9]).

The loading is applied until reaching $\epsilon_y = \Delta_y/height = 0.2$ (pulling) or $\gamma = \Delta_x/height = 0.2$ (shearing), where Δ_y is the displacement following the y-axis, Δ_x is the displacement following the x-axis, and *height* is the dimension of the sample in the y-axis. The mechanical problem is also solved with the finite element solver MOOSE [57]. An example of microstructure loading is depicted in Figure 12.

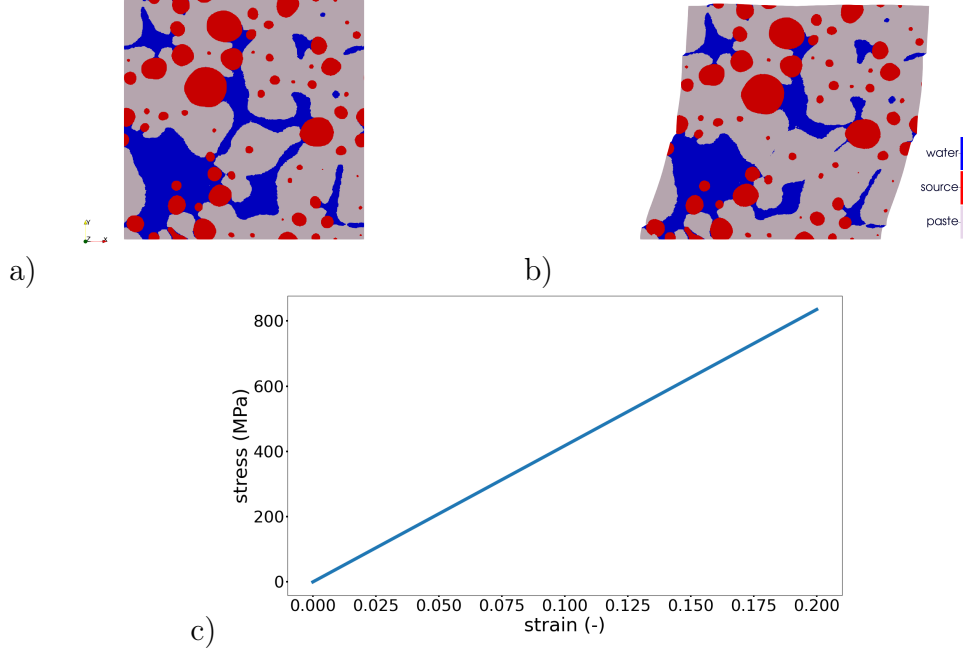


Figure 12: Example of the prediction of the shear modulus for a $w/c = 0.5$ configuration: a) the composite material is b) loaded, and the parameter is estimated from c) the strain-stress curve.

Then, the mechanical parameters of the sample are computed by homogenization of the stresses and the strains in the domain. The Young modulus E_h is determined with the traction test by interpolating the relation $\sigma_{yy} = E_h \cdot \epsilon_y$, where σ_{yy} is the mean stress in the source and paste phases and ϵ_y is the loading condition. The Shear modulus G_h is determined with the shearing test by interpolating the relation $\sigma_{xy} = G_h \cdot \gamma$, where σ_{xy} is the mean stress in the source and paste phases and γ is the loading condition. The Poisson's ratio ν_h can be interpolated with a traction test without periodic conditions (not conducted herein) and the Bulk modulus K_h can also be interpolated with an isotropic loading test (not conducted herein). These

parameters could also be interpolated from the interpolated Young and Shear moduli ($\nu_h = E_h/(2 \cdot G_h) - 1$ and $K_h = (E_h \cdot G_h)/(9G_h - 3E_h)$).

The framework presented herein could be extended to determine numerically the yield envelope of the sample. To achieve this, each distinct phase should be characterized by a plasticity criterion, and the sample should be subjected to various mechanical loading paths until the overall mechanical behavior deviates from linearity (after significant plastic deformation occurs locally) [79, 80].

4.2. Results

The evolution of the homogenized Young modulus E_h and Shear modulus G_h is available in Figure 13. The cases $w/c = 0.3$ and $w/c = 0.5$ are compared to the results from [48] and the intrinsic value for the paste phase, dominant in the domain and representing the weaker phase (pore/water excluded). Moreover, a realistic microstructure obtained by Scanning Electron Microscope observation of a $w/c = 0.5$ sample, from [6], is used as an input of the homogenization method for comparison purposes.

It is worth noting that the hydration that ensures the mechanical continuity varies in the repeated simulation, see the variation in Figure 8. For comparison purposes, the curves are then shifted to a common point time_{cont} , which represents the mechanical continuity time for each individual simulation.

As expected, the different moduli (Young and Shear) increase with the hydration process. As the chemical process occurs, bonds are generated between the aggregates, and the mechanical properties of the sample harden. Similar to the tendencies observed in [48], the evolution consists of two stages:

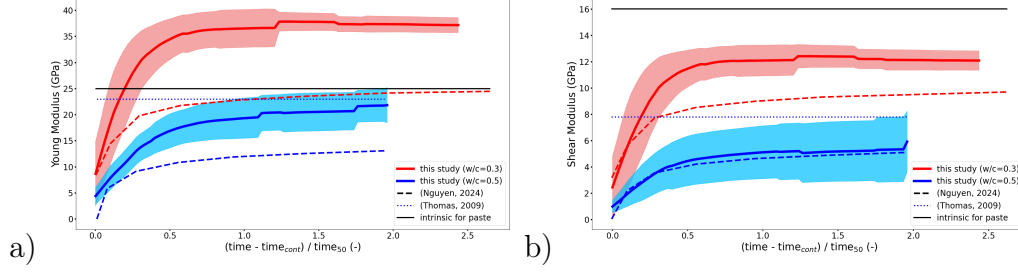


Figure 13: Time evolution of the homogenized a) Young modulus E_h and b) Shear modulus G_h in the cases $w/c = 0.3$ and 0.5 .

an initial rapid phase followed by a slower final phase. This curve is correlated to the hydration evolution depicted in Figure 6. The microstructure remains weak at the initial mechanical continuity point (when there exists a continuous paste+source phase between the top and the bottom of the sample). As shown in Figure 5, the bonds between the aggregates remain small. However, the bond sizes increase with the hydration, and it reinforces the sample.

The results for $w/c = 0.5$ obtained by the PF formulation appear closer to the estimated moduli from the real microstructure obtained by [6] than the results from [48]. Indeed, the microstructure computed with the *CEMHYD3D* description is more discrete, and the different phases are less continuous than the ones obtained with a PF formulation. These localizations generate weak points in the *CEMHYD3D* microstructure and weaken the sample. Furthermore, it has been pointed out in Figure 7 that the *CEMHYD3D* formulation overestimates the volume fraction of the pore, weakening the microstructure. Because of these weakening origins, the moduli of the homogenized *CEMHYD3D* microstructure appear much smaller than the intrinsic

value of the cement paste (weakest phase after pore/water and dominant in the microstructure). The PF formulation appears more suitable than the *CEMHYD3D* description.

The $w/c = 0.3$ microstructure appears stiffer than the $w/c = 0.5$ microstructure for the different moduli (Young and Shear). Indeed, Figure 5 emphasizes there are more source inclusions in the case $w/c = 0.3$. These inclusions are stiffer, see Table 2, and affect the mechanical behavior of the sample. As a reminder, the saturation limit has been defined as $w/c = 0.42$. This limit is defined as the maximal source quantity with full hydration. If w/c is smaller, there are remaining source inclusions (rigid phase) after the hydration. If w/c is larger, there is not enough source to produce a saturation of the hydration.

Similar to the previous results, the PF simulations appear reproducible. The largest variations are located in the evolution of the Shear modulus. Indeed, Figure 5 depicts the fact that the initial configuration (position of the source particles) is heterogeneous. The Shear modulus is more sensitive to such irregular aspects of the microstructure, the pores acting as weakness points. In the same vein, it is relevant to emphasize the fact that the variance for the $w/c = 0.5$ configuration is larger than for the $w/c = 0.3$ configuration. Indeed, the irregular aspect of the initial configuration is even more visible for $w/c = 0.5$ as there is less cement source/more pore space. The quality of the results would be better with a more homogeneous initial configuration, considering another algorithm for the generation.

The results obtained for the Young modulus of the hydrated sample are compared with the values available in the literature for distinct w/c values

in Figure 14. It is important to point out that these data have been obtained with a PF formulation + computational homogenization [33], a CA description + computational homogenization [48, 70, 81, 82, 83, 84, 85], a computational homogenization based on experimental observations [86, 87, 88, 89, 90, 91], a several-steps homogenization model [56, 92], or by experiments [48, 50, 92]. Moreover, sample characteristics are not always consistent in this dataset. For instance, the species distribution, the preparation methods, or the intrinsic mechanical parameters for the distinct phases are not similar. The properties of the composite material appear to be widely impacted by these fluctuations.

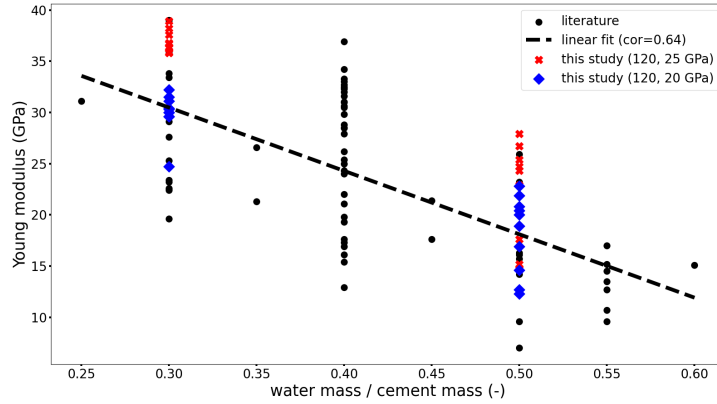


Figure 14: Dataset of the Young modulus of the hydrated concrete material for distinct w/c ratios. Different computation homogenization has been conducted from the microstructure evolution depicted herein, considering (Y_{source}, Y_{paste}) .

First of all, it appears that, at a given w/c , a large distribution of the Young modulus of the hydrated sample is available in the literature. This parameter is deeply affected by the prediction method (modelization or experimental). In the case of the modelization, the homogenized Young mod-

ulus depends on the intrinsic value considered for the different phases and on the quality of the microstructure estimation. For instance, it has been emphasized in Figure 7 that the CA approach tends to overestimate the pore space (weak phase) during the hydration process. Then, it is not surprising to obtain larger values employing similar intrinsic parameters with a PF formulation. Indeed, the approach employed herein performs better in the description of the hydrated microstructure, predicting less pore space. Moreover, the C-S-H material is a heterogeneous phase with, in particular, a variation in the packing density [55, 56, 66]. This fluctuation has an impact on the local properties of the cement material [93] and may generate some weak regions. The Young modulus estimated through a numerical homogenization method after the PF prediction of the microstructure appears in the upper envelope of the available dataset. However, the quality of the PF prediction appears to increase by considering the lower boundary depicted in [48] for the intrinsic Young modulus of the C-S-H phase ($Y_{paste} = 20$ GPa).

Obviously, the prediction of the method presented herein would increase, considering a 3D microstructure, capturing the fingering growth pattern of the paste, employing a more realistic size distribution and shapes for the source particle, or by adding the supplementary phases and their physics.

5. Discussion

The numerical laboratory approach, describing explicitly the microstructure, provides a suitable framework for investigating the hydration process of concrete materials. It appears that the currently most employed formulation is based on discrete models, such as *CEMHYD3D*. However, the co-

efficients used are largely derived from semi-empirical methods. Moreover, the intrinsic nature of CA induces that the microstructure obtained is highly heterogeneous, and different concentrations of species at one location in the pore water can not be modeled. Consequently, a physics-based description, the PF formulation, seems more adequate. For instance, this work emphasizes that the PF method reproduces the microstructure evolution driven by chemical processes more accurately than the CA model.

In the same vein, it is worth comparing the framework depicted herein with the analytical homogenization methods available in the literature. The difference is the fact that a PF describes the microstructure explicitly, while the homogenization approach requires making assumptions on the shape, the proportion, and the location of the distinct phases. Even if the microstructure is described, it is not in an explicit manner. It has been emphasized that the microstructure is pivotal for the estimation of the material behavior (mechanics, chemistry, or hydrology) [46, 94, 95], emphasizing the importance of capturing it accurately. Moreover, the PF approach enables the couplings with other physics, such as the temperature, the stress, or the presence of a fluid transport, while such considerations remain difficult through constitutive relations for the hydration of the material, a key ingredient of the prediction by homogenization.

Nevertheless, the computational cost of the PF simulations remains huge; the resolution of a 2D simulation (microstructure evolution prediction and mechanical behavior interpolation, depicted herein) lasts approximately 10 hours on a regular computer (Intel(R) Core(TM) i5-10210U CPU @ 1.60GHz, 8 Go RAM). However, numerous methods may be employed to diminish the

resources required, allowing the use of the PF description for 3D problems, considering multi-physics [96, 97]. Future work should extend this model to 3D to more accurately capture the complex pore network connectivity and tortuosity, which are known to be critical for transport properties and may further refine the predicted percolation threshold and mechanical response.

6. Conclusion

This paper presents a Phase-Field formulation of the hydration of a concrete material, describing explicitly the microstructure and its evolution. In particular, the proposed physics-based description—featuring a revised free-energy potential and distinct equilibrium constants—is compared to experimental observations and to a semi-empirical Cellular Automata approach available in the literature. Considering two distinct boundary value problems ($w/c = 0.3$ and 0.5), the Phase-Field formulation appears to reproduce the kinetics, phase distribution, and organization of the microstructure. It has also been shown that the Cellular Automata approach tends to overestimate pore space during hydration, which is not observed with the formulation depicted herein.

Once the microstructural evolution is estimated with the Phase-Field model, the resulting microstructures are used as inputs to a computational homogenization scheme to predict the evolution of the mechanical properties of the material. Mechanical performance appears to be captured with more precision through the Phase-Field formulation than through the Cellular Automata description. In particular, the overestimation of porosity inherent to Cellular Automata leads to an artificially weakened composite, whereas the

Phase-Field model provides a more physically consistent estimate.

Although this work focuses on the mechanical response of the hydrating material, the framework depicted herein can readily be extended to other coupled physics. With appropriate constitutive laws, the same microstructural predictions could be used to assess thermal or hydraulic behavior, offering a more comprehensive multiphysics view of cementitious materials.

The Phase-Field description therefore provides a promising foundation for improving our understanding of hydration at the microscale and for exploring the influence of key parameters such as particle size distribution or chemical composition. Although further validation and application to a wider set of conditions are still needed, the ability to anticipate mechanical behavior directly from the evolution of the simulated microstructure suggests a useful complementary tool alongside traditional 28-day testing protocols.

7. Code availability

Some examples of scripts used are available on Github: https://github.com/AlexSacMorane/PF_CementHydration.

8. Acknowledgements

This research has been partially funded by the Fonds Spécial de Recherche (FSR) and by the Wallonia-Bruxelles Federation. The work has also received funding from the NSF project CMMI-2042325.

Appendix A. Particle Size Distribution of the source

To ensure the model is representative of the experiments, it is important to reproduce most of the parameters available. Concerning the hydration problem, the particle size distribution of the source grains represents a parameter with a large impact on the hydration kinetics and the microstructure evolution obtained.

In the context of a numerical analog, the investigation pursued employed a particle size distribution from a database available [9, 65], see Table A.3. This Table presents the mass and number ratios of different radius bins (from $0.5 \mu m$ to $36.5 \mu m$). Between the limits of the bins, a uniform distribution is assumed for the radius. However, the PF formulation induces a minimal size for grains to remain stable. Indeed, if the particle size is smaller than the minimal size ($\sim 2 \times \delta$, where δ is the interface width), the maximum value of the phase variable is smaller than 0.5, dissolution ($\eta \rightarrow 0$) occurs due to the PF formulation. As emphasized in Table 1, the mesh size Δ is $0.2 \mu m$, limiting the minimal radius to $2 \times \delta = 2 \times 6\Delta = 2.4 \mu m$. The particle size distribution is then modified to consider this minimal size restriction, see Table A.3.

Radius (μm)	Mass (%) initial	Number (%) initial	Number (%) from $2.5 \mu m$
0.5	13.5	95.8	not considered
1.5	13.0	3.4	
2.5	9.5	0.5	
3.5	7.3	0.2	18.6

4.5	6.1	0.1	7.3
5.5	5.1	not enough (< 0.1)	3.3
6.5	4.2		1.7
7.5	3.8		1.0
8.5	3.4		0.6
9.5	2.8		0.4
10.5	2.6		0.2
11.5	2.3		0.2
12.5	2.1		0.1
13.5	1.9		0.1
14.5	1.9		0.1
15.5	2.3		0.1
17.5	3.5	not enough (< 0.1)	not enough (< 0.1)
20.5	2.7		
23.5	4.5		
30.5	3.6		
36.5	4.0		

Table A.3: Particle size distribution for the cement CCL 133.

The conversion between the mass fraction and the number fraction has been obtained by considering that the shape of the particle is a sphere and by following the scheme described in Algorithm 1.

Algorithm 1 Convert a mass ratio V_i to a number ratio N_i .

assume there is $n_0 = 1$ particle for the size 0

for all size $i \in \text{bins}$ (except $i = 0$) **do**

 compute the number of particle n_i for the size i $\triangleright \frac{n_i}{n_0} = \frac{V_i}{V_0} \left(\frac{R_0}{R_i} \right)^3$

end for

Compute the total number of particles n_t $\triangleright n_t = \sum_i n_i$

for all size $i \in \text{bins}$ **do**

 compute the number ratio N_i for the size i $\triangleright N_i = \frac{n_i}{n_t}$

end for

Appendix B. Sensitivity analysis of the coefficient α_{CSH}

As mentioned in Subsection 2.1, the conversion terms α_{CSH}/α_{CS} are correlated, but the values remain unknown. In the absence of experimental data available, a sensitivity analysis is then conducted to determine the value of α_{CSH} (and α_{CS} through Equation 6). The results for the configuration $w/c = 0.5$ are available in Figure B.15.

It appears that a small α_{CSH} induces the fact that the source particles are significantly dissolved before the precipitation of the paste, see the Figure B.15a), not in agreement with the experimental observations [43, 44]. Indeed, the solute c produced by the dissolution of the source is not sufficient to generate a supersaturation state. On the contrary, a large α_{CSH} instigates negative values for the solute concentration c , see the Figure B.15c). This state is explained by the large quantity of solute required for the paste precipitation. Finally, the value $\alpha_{CSH} = 3$ is employed herein as it seems to verify the experimental observations (small source dissolution at the supersaturation

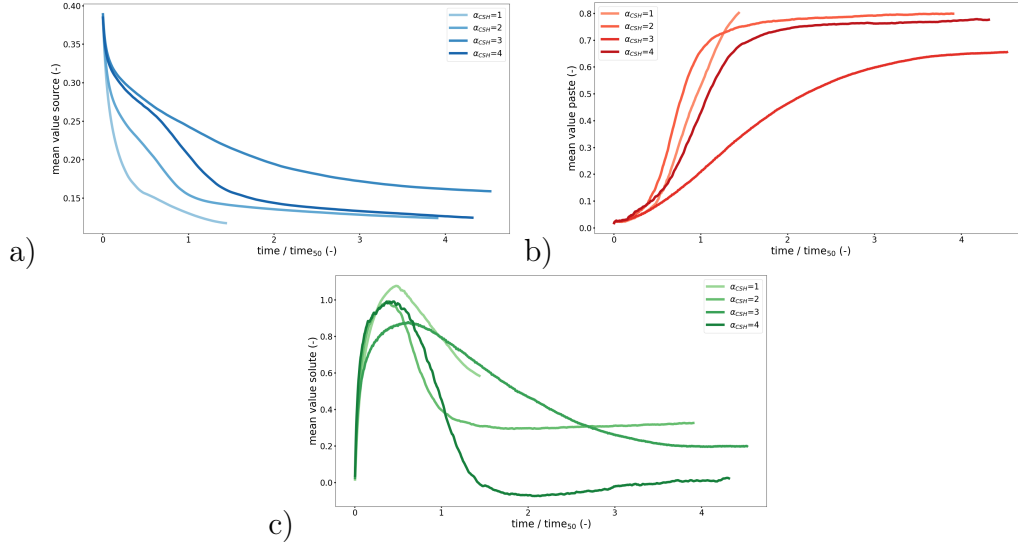


Figure B.15: Evolution of the mean value of the variable a) $C3S$, b) CSH , and c) c for different a_{CSH} coefficients ($w/c = 0.5$).

state and positive value for the solute concentration).

Appendix C. Definition of the normalized two-point correlation function

In the goal of comparing microstructures, a normalized two-point correlation function has been developed [71]. Considering an $M \times N$ image of the microstructure, the two-point correlation function is obtained through Equation C.1.

$$S(x, y) = \sum_{i=1}^{M-x} \sum_{j=1}^{N-y} \frac{I(i, j)I(x + i, y + j)}{(M - x)(N - y)} \quad (C.1)$$

where $I(i, j) = 1$ if the voxel located at (i, j) represents the phase of interest, $= 0$ otherwise. The values x and y are the pixel offsets investigated

and can be converted into a radial distance r [98]:

$$S(r) = \frac{1}{2r+1} \sum_{l=0}^{2r} S\left(r, \frac{\pi l}{4r}\right) \quad (\text{C.2})$$

It appears that the value $S(0)$ represents the volume fraction of the investigated phase. To compare the microstructure at different volume fractions, the two-point correlation function is normalized with Equation C.3.

$$N(r) = \frac{S(r) - S(0)S(0)}{S(0) - S(0)S(0)} \quad (\text{C.3})$$

Appendix D. Correlation functions for repeated configurations

The two-point correlation function is a common tool to provide insights into the microstructure [71]. For instance, Figure 10 depicts the evolution of the functions during the hydration process, considering an individual simulation. However, the repeatability is not emphasized, for clarity reasons. This Appendix and Figure D.16 investigate this aspect in the case $w/c = 0.3$.

It appears in Figure D.16a) and c) that the functions are overlaid for the initial and final states. The initial state of the configuration is unsurprisingly repeatable, while it is comforting to verify that the final state is similar in the different simulations. Concerning the intermediate state depicted in Figure D.16b), the range of the functions is narrow. In particular, two groups of curves appear. Indeed, Figure 6 emphasizes the variation of the hydration kinetics, in particular for the intermediate state ($t/t_{50} = 0.41 \sim h = 30\%$). Some simulations depict faster kinetics compared to the others, explaining the two groups. The prediction of the microstructure evolution appears reproducible.

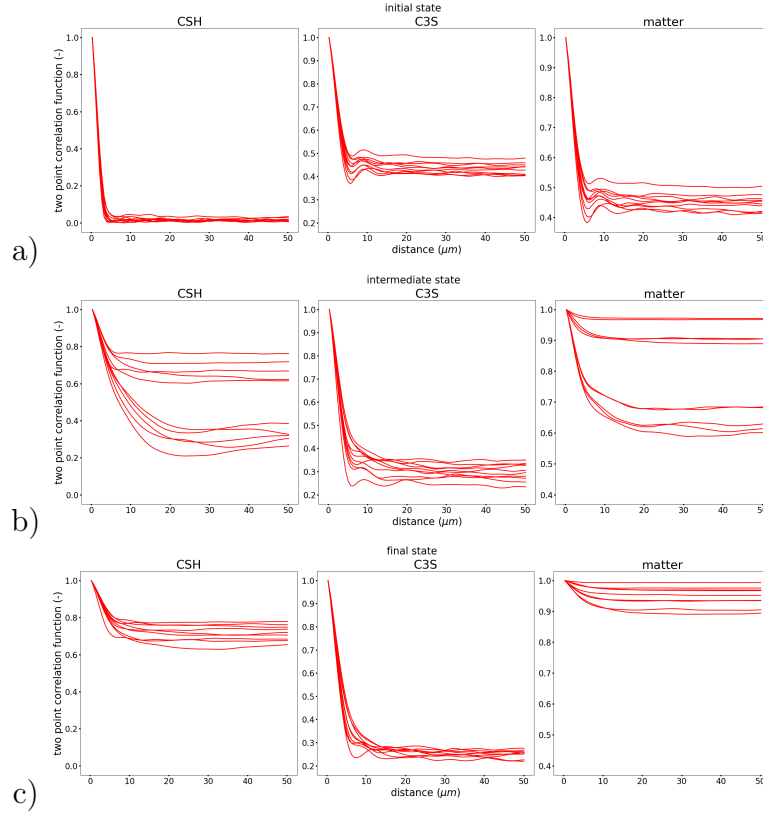


Figure D.16: Evolution of the correlation function for the different phases (paste, source, paste+source) in the case $w/c = 0.3$ for $t/t_{50} =$ a) 0.04, b) 0.41, and c) 0.83. The configuration has been repeated ten times.

References

- [1] M. Nithurshan and Y. Elakneswaran, “A systematic review and assessment of concrete strength prediction models,” *Case Studies Constr. Mater.*, vol. 18, p. e01830, 2023.
- [2] I. H. Shah, S. A. Miller, D. Jiang, and R. J. Myers, “Cement substitution with secondary materials can reduce annual global co2 emissions by up to 1.3 gigatons,” *Nat. Commun.*, vol. 13, p. 5758, 2022.

- [3] R. Feret, “sur la compacité des mortiers hydrauliques,” *Annales des ponts et chaussées*, 1892.
- [4] S. E. Chidiac, F. Moutassem, and F. Mahmoodzadeh, “Compressive strength model for concrete,” *Mag. Concr. Res.*, vol. 65, pp. 557–572, 2013.
- [5] F. De Larrard, *Concrete Mixture Proportioning: A Scientific Approach*. CRC Press, 1999.
- [6] J. Thomas, H. Jennings, and J. Chen, “Influence of nucleation seeding on the hydration mechanisms of tricalcium silicate and cement,” *J. Phys. Chem. C*, vol. 113, pp. 4327–4334, 2009.
- [7] S. Kawashima, P. Hou, D. J. Corr, and S. P. Shah, “Modification of cement-based materials with nanoparticles,” *Cem. Concr. Composites*, vol. 36, pp. 8–15, 2013.
- [8] G. Lefever, D. Aggelis, N. De Belie, M. Raes, T. Hauffman, D. Van Hemelrijck, and D. Snoeck, “The influence of superabsorbent polymers and nanosilica on the hydration process and microstructure of cementitious mixtures,” *Mat.*, vol. 13, pp. 1–16, 2020.
- [9] V. T. Nguyen, S. Y. Lee, S.-Y. Chung, J.-H. Moon, and D. J. Kim, “Effects of cement particle distribution on the hydration process of cement paste in three-dimensional computer simulation,” *Constr. Build. Mater.*, vol. 311, p. 125322, 2021.

- [10] T. Powers and T. Brownyard, “Studies of the physical properties of hardened portland cement paste,” in *PCA Bulletin No 22. American Concrete Institute*, pp. 101–132, 1946.
- [11] N. Agofack, *Comportement des ciments pétroliers au jeune âge et intégrité des puits*. PhD thesis, Université Paris-Est, 2015.
- [12] M. Samudio, *Modelling of an oil well cement paste from early age to hardened state: hydration kinetics and poromechanical behaviour*. PhD thesis, Université Paris-Est, 2017.
- [13] B. Budiansky, “On the elastic moduli of some heterogeneous materials,” *J. Mech. Phys. Solids*, vol. 13, pp. 223–227, 1965.
- [14] R. McLaughlin, “A study of the differential scheme for composite materials,” *Int. J. Eng. Sci.*, vol. 15, pp. 237–244, 1977.
- [15] S. Ghabezloo, “Association of macroscopic laboratory testing and micromechanics modelling for the evaluation of the poroelastic parameters of a hardened cement paste,” *Cem. Concr. Res.*, vol. 40, pp. 1197–1210, 2010.
- [16] J. C. Halpin and J. L. Kardos, “The halpin-tsai equations: A review,” *Polymer Eng. Sci.*, vol. 16, pp. 344–352, 1976.
- [17] B. Pichler, C. Hellmich, and J. Eberhardsteiner, “Spherical and acicular representation of hydrates in a micromechanical model for cement paste: Prediction of early-age elasticity and strength,” *Acta Mech.*, vol. 203, pp. 137–162, 2009.

- [18] J. D. Eshelby, “The determination of the elastic field of an ellipsoidal inclusion, and related problems,” *Proc. R. Soc. A*, vol. 241, pp. 376–396, 1957.
- [19] R. Hill, “A self-consistent mechanics of composite materials,” *J. Mech. Phys. Solids*, vol. 13, pp. 213–222, 1965.
- [20] T. Mori and K. Tanaka, “Average stress in matrix and average elastic energy of materials with misfitting inclusions,” *Acta Metall.*, vol. 21, pp. 571–574, 1973.
- [21] B. Pichler and C. Hellmich, “Upscaling quasi-brittle strength of cement paste and mortar: A multi-scale engineering mechanics model,” *Cem. Concr. Res.*, vol. 41, pp. 467–476, 2011.
- [22] B. Pichler, C. Hellmich, J. Eberhardsteiner, J. Wasserbauer, P. Termkhajornkit, R. Barbarulo, and G. Chanvillard, “Effect of gel-space ratio and microstructure on strength of hydrating cementitious materials: An engineering micromechanics approach,” *Cem. Concr. Res.*, vol. 45, pp. 55–68, 2013.
- [23] B. Pichler, S. Scheiner, and C. Hellmich, “From micron-sized needle-shaped hydrates to meter-sized shotcrete tunnel shells: Micromechanical upscaling of stiffness and strength of hydrating shotcrete,” *Acta Geotech.*, vol. 3, pp. 273–294, 2008.
- [24] J. F. Wang, L. W. Zhang, and K. M. Liew, “Multiscale simulation of mechanical properties and microstructure of cnt-reinforced cement-based

- composites,” *Comput. Methods Appl. Mech. Eng.*, vol. 319, pp. 393–413, 2017.
- [25] D. P. Bentz, E. J. Garboczi, J. W. Bullard, C. Ferraris, N. Martys, and P. E. Stutzman, *Significance of tests and properties of concrete and concrete-making materials*, ch. Virtual Testing of Cement and Concrete. ASTM International, 2006.
- [26] K. van Breugel, “Numerical simulation of hydration and microstructural development in hardening cement-based materials: (i) theory,” *Cem. Concr. Res.*, vol. 25, pp. 319–331, 1995.
- [27] N. Holmes, D. Kelliher, and M. Tyrer, “Simulating cement hydration using hyd cem,” *Constr. Build. Mater.*, vol. 239, p. 117811, 2020.
- [28] J. W. Bullard, “Approximate rate constants for nonideal diffusion and their application in a stochastic model,” *J. Phys. Chem. A*, vol. 111, pp. 2084–2092, 2007.
- [29] S. Bishnoi and K. Scrivener, “ μic : A new platform for modelling the hydration of cements,” *Cem. Concr. Res.*, vol. 39, pp. 266–274, 2009.
- [30] C. Pignat, P. Navi, and K. Scrivener, “Simulation of cement paste microstructure hydration, pore space characterization and permeability determination,” *Mater. Struct.*, vol. 38, pp. 459–466, 2005.
- [31] L. Nguyen-Tuan, F. Kleiner, C. Rößler, and H.-M. Ludwig, “Numerical simulation of model cement hydration using level set based method,” *Cem. Concr. Res.*, vol. 186, p. 107674, 2024.

- [32] B. J. Kooi, “Extension of the johnson-mehl-avrami-kolmogorov theory incorporating anisotropic growth studied by monte carlo simulations,” *Phys. Rev. B*, vol. 73, p. 054103, 2006.
- [33] T. Petersen, P.-L. Valdenaire, R. Pellenq, and F.-J. Ulm, “A reaction model for cement solidification: Evolving the C–S–H packing density at the micrometer-scale,” *J. Mech. Phys. Solids*, vol. 118, pp. 58–73, 2018.
- [34] N. Moelans, B. Blanpain, and P. Wollants, “An introduction to phase-field modeling of microstructure evolution,” *Calphad: Comp. Coupling of Phase Diagrams and Thermochemistry*, vol. 32, pp. 268–294, 2008.
- [35] T. Takaki, “Phase-field modeling and simulations of dendrite growth,” *ISIJ Int.*, vol. 54, pp. 437–444, 2014.
- [36] A. Guével, H. Rattez, and M. Veveakis, “Viscous phase-field modeling for chemo-mechanical microstructural evolution: application to geomaterials and pressure solution,” *Int. J. Solids Struct.*, vol. 207, pp. 230–249, 2020.
- [37] H. Li, F. Wang, Y. Wang, Y. Yuan, G. Feng, H. Tian, and T. Xu, “Phase-field modeling of coupled reactive transport and pore structure evolution due to mineral dissolution in porous media,” *J. Hydrol.*, vol. 619, p. 129363, 2023.
- [38] A. Sac-Morane, M. Veveakis, and H. Rattez, “A phase-field discrete element method to study chemo-mechanical coupling in granular materials,” *Comput. Methods Appl. Mech. Eng.*, vol. 424, p. 116900, 2024.

- [39] A. Sac-Morane, H. Rattez, and M. Veveakis, “Importance of precipitation on the slowdown of creep behavior induced by pressure-solution,” *J. Eng. Mech.*, vol. 151, p. 04025025, 2025.
- [40] J. Ulloa, J. Wambacq, R. Alessi, E. Samaniego, G. Degrande, and S. Francois, “A micromechanics-based variational phase-field model for fracture in geomaterials with brittle-tensile and compressive-ductile behavior,” *J. Mech. Phys. Solids*, vol. 159, p. 104684, 2021.
- [41] J. Xing and C. Zhao, “A hydro-mechanical phase field model for hydraulically induced fractures in poroelastic media,” *Comput. Geosci.*, vol. 159, p. 105418, 2023.
- [42] F. Wu, A. Sac-Morane, H. Rattez, M. Veveakis, and M. Hu, “Onset of reactive brittle cracking in sandstones: Dem-informed phase-field modeling,” *Int. J. Rock Mech. Min. Sci.*, vol. 196, p. 106319, 2025.
- [43] J. Bullard, H. Jennings, R. Livingston, A. Nonat, G. Scherer, J. Schweitzer, K. Scrivener, and J. Thomas, “Mechanisms of cement hydration,” *Cem. Concr. Res.*, vol. 41, pp. 1208–1223, 2011.
- [44] K. L. Scrivener, P. Juilland, and P. J. M. Monteiro, “Advances in understanding hydration of portland cement,” *Cem. Concr. Res.*, vol. 78, pp. 38–56, 2015.
- [45] A. Guével, H. Rattez, and M. Veveakis, “Morphometric description of strength and degradation in porous media,” *Int. J. Solids Struct.*, vol. 241, p. 111454, 2022.

- [46] W. Lindqwister, J. Peloquin, L. Dalton, K. Gall, and M. Veveakis, “Predicting compressive stress-strain behavior of elasto-plastic porous media via morphology-informed neural networks,” *Com. Eng.*, vol. 4, p. 73, 2025.
- [47] H. Isleem, D. Augustino, A. Mohammed, A. Najemalden, P. Jagadesh, S. Qaidi, and M. Sabri, “Finite element, analytical, artificial neural network models for carbon fibre reinforced polymer confined concrete filled steel columns with elliptical cross sections,” *Front. Mater.*, vol. 9, pp. 1–18, 2023.
- [48] V. T. Nguyen, S. Y. Lee, S. Yoon, and D. J. Kim, “A comprehensive study on predicting the elastic modulus and poisson ratio of hardened cement pastes via micro-scale cement hydration simulations,” *Case Studies Constr. Mater.*, vol. 20, p. e03285, 2024.
- [49] A. Alavoine, P. Dangla, and J.-M. Pereira, “Fast fourier transform-based homogenisation of gas hydrate bearing sediments,” *Géotech. Lett.*, vol. 10, pp. 367–376, 2020.
- [50] I. Maruyama and G. Igarashi, “Cement reaction and resultant physical properties of cement paste,” *J. Advanced Concr. Techn.*, vol. 12, pp. 200–213, 2014.
- [51] H. F. W. Taylor, *Cement chemistry*. ICE Publishing, 1997.
- [52] Z. Zhang, F. Han, and P. Yan, “Modelling the dissolution and precipitation process of the early hydration of c3s,” *Cem. Concr. Res.*, vol. 136, p. 106174, 2020.

- [53] J. W. Bullard and R. J. Flatt, “New insights into the effect of calcium hydroxide precipitation on the kinetics of tricalcium silicate hydration,” *J. Am. Ceram. Soc.*, vol. 93, pp. 1894–1903, 2010.
- [54] K. Ioannidou, K. J. Krakowiak, M. Bauchy, C. G. Hoover, E. Masoero, S. Yip, F. J. Ulm, P. Levitz, R. J. Pellenq, and E. Del Gado, “Mesoscale texture of cement hydrates,” *Proc. Natl Acad. Sci. of the United States of Am.*, vol. 113, pp. 2029–2034, 2016.
- [55] K. Ioannidou, R. J. Pellenq, and E. Del Gado, “Controlling local packing and growth in calcium-silicate-hydrate gels,” *Soft Matter*, vol. 10, p. 1121, 2014.
- [56] C. Hu and Z. Li, “Micromechanical investigation of portland cement paste,” *Constr. Build. Mater.*, vol. 71, pp. 44–52, 2014.
- [57] C. Permann, D. Gaston, D. Andrš, R. Carlsen, F. Kong, A. Lindsay, J. Miller, J. Peterson, A. Slaughter, R. Stogner, and R. Martineau, “MOOSE: Enabling massively parallel multiphysics simulation,” *SoftwareX*, vol. 11, p. 100430, 2020.
- [58] D. Schwen, L. Aagesen, J. Peterson, and M. Tonks, “Rapid multiphase-field model development using a modular free energy based approach with automatic differentiation in MOOSE,” *Comput. Mater. Sci.*, vol. 132, pp. 36–45, 2017.
- [59] S. Allen and J. Cahn, “A microscopic theory for antiphase boundary motion and its application to antiphase domain coarsening,” *Acta Metall.*, vol. 27, pp. 1085–1095, 1979.

- [60] M. Mainguy, C. Tognazzi, J. Torrenti, and F. Adenot, “Modelling of leaching in pure cement paste and mortar,” *Cem. Concr. Res.*, vol. 30, pp. 83–90, 2000.
- [61] A. Atkinson and A. Nickerson, “The diffusion of ions through water-saturated cement,” *J. Mater. Sci.*, vol. 19, pp. 3068–3078, 1984.
- [62] C. Liu, C. Qian, R. Qian, Z. Liu, H. Qiao, and Y. Zhang, “Numerical prediction of effective diffusivity in hardened cement paste between aggregates using different shapes of cement powder,” *Constr. Build. Mater.*, vol. 223, pp. 806–816, 2019.
- [63] H. De Sousa and L. Rebelo, “A continuous polydisperse thermodynamic algorithm for a modified flory–huggins model: The (polystyrene + nitroethane) example,” *J. Polym. Sci. Part B: Polym. Phys.*, vol. 38, pp. 501–551, 2000.
- [64] L. Chen, “Phase-field models for microstructure evolution,” *Annual Rev. Mater. Sci.*, vol. 32, pp. 113–140, 2002.
- [65] NIST, “Cement images and psds available for microstructure modeling,” 2005.
- [66] A. Goyal, K. Ioannidou, C. Tiede, P. Levitz, R. J. Pellenq, and E. D. Gado, “Heterogeneous surface growth and gelation of cement hydrates,” *J. Phys. Chem. C*, vol. 124, pp. 15500–15510, 2020.
- [67] M. Castro, “Phase-field approach to heterogeneous nucleation,” *Phys. Rev. B*, vol. 67, p. 035412, 2003.

- [68] M. Sun, G. Geng, D. Xin, and C. Zou, “Molecular quantification of the decelerated dissolution of tri-calcium silicate (c3s) due to surface adsorption,” *Cem. Concr. Res.*, vol. 152, p. 106682, 2022.
- [69] M. Kelm, S. Gärttner, C. Bringedal, B. Flemisch, P. Knabner, and N. Ray, “Comparison study of phase-field and level-set method for three-phase systems including two minerals,” *Comput. Geosci.*, vol. 26, pp. 545–570, 2022.
- [70] C. J. Haecker, E. J. Garboczi, J. W. Bullard, R. B. Bohn, Z. Sun, S. P. Shah, and T. Voigt, “Modeling the linear elastic properties of portland cement paste,” *Cem. Concr. Res.*, vol. 35, pp. 1948–1960, 2005.
- [71] D. P. Bentz, “Quantitative comparison of real and cemhyd3d model microstructures using correlation functions,” *Cem. Concr. Res.*, vol. 36, pp. 259–263, 2006.
- [72] S. Torquato, *Microstructure and Macroscopic Properties*. Springer, 2002.
- [73] L. E. Dalton, D. Crandall, and M. Pour-Ghaz, “Supercritical, liquid, and gas co₂ reactive transport and carbonate formation in portland cement mortar,” *Int. J. Greenhouse Gas Control*, vol. 116, p. 103632, 2022.
- [74] E. A. Chavez Panduro, B. Cordonnier, K. Gawel, I. Borge, J. Iyer, S. A. Carroll, L. Michels, M. Rogowska, J. A. McBeck, H. O. Sorensen, S. D. C. Walsh, F. Renard, A. Gibaud, M. Torsaeter, and D. W. Breiby, “Real time 3d observations of portland cement carbonation at co₂ storage conditions,” *Environ. Sci. Technol.*, vol. 54, pp. 8323–8332, 2020.

- [75] A. Fabbri, J. Corvisier, A. Schubnel, F. Brunet, B. Goffé, G. Rimmele, and V. Barlet-Gouédard, “Effect of carbonation on the hydro-mechanical properties of portland cements,” *Cem. Concr. Res.*, vol. 39, pp. 1156–1163, 2009.
- [76] R. Alizadeh, J. J. Beaudoin, and L. Raki, “Viscoelastic nature of calcium silicate hydrate,” *Cem. Concr. Composites*, vol. 32, pp. 369–376, 2010.
- [77] Z. Hu, A. Hilaire, J. Ston, M. Wyrzykowski, P. Lura, and K. L. Scrivener, “Intrinsic viscoelasticity of c-s-h assessed from basic creep of cement pastes,” *Cem. Concr. Res.*, vol. 121, pp. 11–20, 2019.
- [78] A. Yahia, A. Perrot, D. Feys, K. Khayat, M. Sonebi, S. Kawashima, and W. Schmidt, “Viscoelastic properties of fresh cement paste: measuring procedures and influencing parameters,” *RILEM Techn. Lett.*, vol. 8, pp. 23–30, 2023.
- [79] M. Lesueur, T. Poulet, and M. Veveakis, “Predicting the yield strength of a 3d printed porous material from its internal geometry,” *Additive Manuf.*, vol. 44, p. 102061, 2021.
- [80] M. Lesueur, H. Rattez, and M. Veveakis, “Influence of cementation on the yield surface of rocks numerically determined from digital microstructures,” *Int. J. Plast.*, vol. 156, p. 103338, 2022.
- [81] Z. Qian, *Multiscale Modeling of Fracture Processes in Cementitious Materials*. PhD thesis, TUDelft, 2012.

- [82] D. Hou, W. Zhang, P. Wang, and H. Ma, “Microscale peridynamic simulation of damage process of hydrated cement paste subjected to tension,” *Constr. Build. Mater.*, vol. 228, p. 117053, 2019.
- [83] X. Li, X. Gu, X. Xia, E. Madenci, X. Chen, and Q. Zhang, “Effect of water-cement ratio and size on tensile damage in hardened cement paste: Insight from peridynamic simulations,” *Constr. Build. Mater.*, vol. 356, p. 129256, 2022.
- [84] B. Yan, H. Jia, E. Yilmaz, X. Lai, P. Shan, and C. Hou, “Numerical study on microscale and macroscale strength behaviors of hardening cemented paste backfill,” *Constr. Build. Mater.*, vol. 321, p. 126327, 2022.
- [85] P. Yu, Z. Ren, Z. Chen, and S. P. A. Bordas, “A multiscale finite element model for prediction of tensile strength of concrete,” *Finite Elements Analysis Design*, vol. 215, p. 103877, 2023.
- [86] M. Lukovic, E. Schlangen, and G. Ye, “Combined experimental and numerical study of fracture behaviour of cement paste at the microlevel,” *Cem. Concr. Res.*, vol. 73, pp. 123–135, 2015.
- [87] H. Zhang, B. Savija, S. C. Figueiredo, M. Lukovic, and E. Schlangen, “Microscale testing and modelling of cement paste as basis for multi-scale modelling,” *Mat.*, vol. 9, p. 907, 2016.
- [88] H. Zhang, B. Savija, M. Lukovic, and E. Schlangen, “Experimentally informed micromechanical modelling of cement paste: an approach coupling x-ray computed tomography and statistical nanoindentation,” *Compos. B Eng.*, vol. 157, p. 109–122, 2019.

- [89] B. Savija, H. Zhang, and E. Schlangen, “Micromechanical testing and modelling of blast furnace slag cement pastes,” *Constr. Build. Mater.*, vol. 239, p. 117841, 2020.
- [90] J. Zhang, J. Wang, W. Li, Q. Yuan, and Y. Gao, “A micromechanical investigation of cement paste through a combination of the x-ray computed tomography and the phase field method,” *J. Build. Eng.*, vol. 84, p. 108449, 2024.
- [91] J. Zhang, W. Li, Q. Yuan, J. Wang, and Y. Gao, “Insights on the representative elementary volume of plain cement paste from a micromechanical perspective,” *J. Build. Eng.*, vol. 100, p. 111741, 2025.
- [92] G. Constantinides and F. J. Ulm, “The effect of two types of c-s-h on the elasticity of cement-based materials: Results from nanoindentation and micromechanical modeling,” *Cem. Concr. Res.*, vol. 34, pp. 67–80, 2004.
- [93] F. Moutassem and S. Chidiac, “Assessment of concrete compressive strength prediction models,” *KSCE J. Civil Eng.*, vol. 20, pp. 343–358, 2016.
- [94] W. Lindqwister, M. Veveakis, and M. Lesueur, “Chemical homogenization for nonmixing reactive interfaces in porous media,” *ACS Omega*, vol. 10, pp. 21553—21567, 2025.
- [95] P. A. Slotte, C. F. Berg, and H. H. Khanamiri, “Predicting resistivity and permeability of porous media using minkowski functionals,” *Transp. Porous Med.*, vol. 131, pp. 705–722, 2020.

- [96] M. Sessin, L. Shi, S. R. Phillpot, and M. R. Tonks, “Phase-field modeling of carbon fiber oxidation coupled with heat conduction,” *Comput. Mater. Sci.*, vol. 204, p. 111156, 2022.
- [97] B. Battas, M. W. Cooper, C. O. Galvin, and M. R. Tonks, “The impact of minor non-stoichiometry on sintering behavior: A phase-field study,” *Comput. Mater. Sci.*, vol. 259, p. 114100, 2025.
- [98] J. G. Berryman, “Measurement of spatial correlation functions using image processing techniques,” *J. Appl. Phys.*, vol. 57, pp. 2374–2384, 1985.